

A Non Linear Spectral Graph Neural Network Simulator for More Stable and Accurate Rollouts

Salman N. Salman,¹ Sergey A. Shteingolts,¹ Ron Levie,² and Dan Mendels^{1, a)}

¹⁾*The Wolfson Department of Chemical Engineering, Technion – Israel Institute of Technology, Haifa 32000, Israel*

²⁾*Faculty of Mathematics, Technion – Israel Institute of Technology, Haifa 32000, Israel*

Molecular dynamics (MD) simulations are a central tool in science and engineering enabling the study of dynamical behavior and the link between microscopic structure and macroscopic function. Their high computational cost, however, has motivated extensive efforts to develop accelerated alternatives. A promising approach is the use of machine-learning-based simulators that allow for substantially larger time steps than conventional MD. Among these, graph neural network (GNN)-based methods have been found to be especially attractive given that they naturally encode the inductive bias of interacting particle systems, however current architectures remain limited in accuracy and stability. In particular, standard message-passing schemes struggle to efficiently propagate long-range information. Here, we investigate whether spectral-GNN simulators can overcome these limitations by explicitly representing a simulated system in a global eigenmode basis, and therefore better capture long-range and collective behavior. Focusing on disordered elastic networks, model systems for complex materials and biological structures such as proteins, we compare spatial, linear spectral, and nonlinear spectral GNN architectures. We find that while spectral representations alone are not sufficient, nonlinear spectral models substantially outperform alternatives. By learning both the time-dependent dynamics and the mixing of eigenmodes, these models more accurately capture the system's slow, global modes, which dominate macroscopic behavior. This leads to a marked reduction in systematic particle-position error and significantly improved prediction of global physical properties.

I. INTRODUCTION

The application of artificial intelligence (AI) has seen rapid growth across the physical sciences and engineering in recent years.^{1–4} Machine learning (ML) and AI related techniques have proven effective in diverse tasks such as force-field development,^{5–8} enhanced sampling,^{9–17} structure prediction,^{18–22} and inverse design.^{23–27} However, the performance of ML models is often strongly dependent on the availability of large, high-quality datasets. This poses a major challenge in domains where data generation is expensive or in data-scarce settings. Furthermore, these models typically struggle to extrapolate beyond their training domain. One potential strategy to mitigate these limitations is to train on dynamical data from the domain of interest.^{28–30}

Data of this kind are often available from simulations and, in some cases, from experiments that resolve dynamical behavior.³¹ The key idea is to train ML models to detect recurring motifs in system dynamics, enabling them to learn physical principles that are not captured by static structures or coarse global features. By leveraging these dynamical regularities, such models can be far more sample-efficient, cutting down the number of systems required for training. Consequently, the overall need for data from costly sources such as experiments, *ab initio* computations, or long-timescale simulations can be greatly reduced.

In this context, neural network simulators (NNS) that predict the time-dependent behavior of a system using a set of input descriptors, are an attractive choice due to their ability to capture and generalize the dynamics of complex systems.^{32–45}

As traditional simulators, those that repeatedly solve Newton's second law, including ones that rely on machine-learned interatomic potentials (MLIPs), are often computationally expensive, NNSs offer a compelling alternative because they can propagate trajectories with step sizes that are approximately 10–1000 times larger than standard MD time steps. NNSs can significantly reduce computational cost, making them particularly useful for tasks such as high-throughput screening.^{36,46,47} Moreover, they can infer a broad range of system properties without explicit supervision and capture temporal evolution. Their end-to-end differentiability⁴⁸ further makes them suitable for gradient-based optimization tasks such as inverse design and materials discovery.⁴⁹ Within ML-based simulators, one widely used and successful architecture is the graph neural network (GNN).⁵⁰ GNNs have demonstrated superior generalization ability compared to non-GNN models and have been highly effective at predicting the dynamics of complex systems.^{30,35–38,51,52} Their success can be attributed to the fact that many physical systems, such as materials and molecules, are naturally represented, or can be represented, as interaction graphs. In such graphs, interactions are learned through local message-passing, where each node aggregates information from its neighbors and processes the ined message using multilayer perceptrons.

GNN simulators are often trained to output a system's position, velocity, or acceleration at the next time step given similar information about previous timesteps.^{30,35–38} By applying a model auto-regressively one can generate a sequence of timesteps called a "rollout." During rollout, prediction errors accumulate at each step, causing accuracy and stability to deteriorate as the rollout length increases. This creates a significant challenge for learning complex dynamics and for accurately predicting system observables, especially when generating trajectories longer than those seen during training. A

^{a)}E-mail: danmendels@technion.ac.il

possible contributor to the loss of accuracy in GNNs is the restriction imposed by the finite neighborhood size used during message passing, which limits their ability to learn long-range interactions. In other words, when a particle's behavior is influenced by others beyond its local connected neighborhood, the model may fail to capture these long-range dynamical effects, leading to reduced predictive accuracy. Incorporating long-range information into the NNS can thus provide a dual benefit: (a) enhanced predictive accuracy, and (b) the capacity to take larger simulation steps, thus limiting the compounding accumulation of errors. To allow the propagation of information from distant nodes additional message-passing layers can be added. However, simply increasing the number of layers often introduces detrimental effects, such as over-smoothing⁵³ or over-squashing.⁵⁴

One possible way to overcome this impediment is to use representations derived from the spectral decomposition of the graph Laplacian, analogous to representing a system in Cartesian space via its Fourier components.⁵⁵ GNNs that operate on this representation are called spectral GNNs. Unlike standard message-passing, spatial models that update the node features directly by aggregating node and edge information from local neighborhoods, spectral GNNs map the node features into the frequency domain via a graph Fourier transform (GFT) which captures both local and global information about the graph. Spectral GNNs project the node features onto the eigenvectors of the graph Laplacian. Then, learnable functions are trained to output weights to amplify or suppress the coefficients (a.k.a. the applied filter) in the spectral domain.

While spatial GNN simulators are ubiquitous in the literature, to the best of our knowledge, there is no treatment of spectral GNNs as simulators. To assess whether incorporating global information via spectral decomposition can improve simulation accuracy, we investigate in this work, using disordered elastic networks (DENs) under compression as a case study, the use of spectral GNN-based simulators to learn complex dynamical behavior. DENs are highly tunable models that can represent a broad range of behaviors and properties. DENs have been used to model a variety of systems, including amorphous solids,⁵⁶ mechanical metamaterials,⁵⁷ biological tissue,⁵⁸ functionality design,^{29,59,60} learning physical systems,^{61,62} and proteins.⁶³

To explore the ability of spectral models to support effective simulation of learned dynamics, we implemented two of the most commonly used approaches in the literature, beginning with ChebNet.⁶⁴ ChebNet is a linear filter where the filter is a polynomial represented in the Chebyshev basis. Then, we use another very common strategy, and that is to use a multi-layer-perceptron (MLP) as a filter in the spectral domain. It is important to note that these classical methods operate diagonally in the spectral domain, where each frequency coefficient is attenuated or amplified separately, without facilitating an interaction between different frequency bands. We find that a substantial boost in accuracy and stability both with respect to these two spectral models and with respect to a standard spatial GNN simulator can be achieved by incorporating a third, recently introduced spectral model.⁶⁵ This model, called nonlinear spectral filter (NLSF), applies an MLP to the

full sequence spectral coefficients, enabling nonlinear mixing of the different frequency modes in the learned representation of the dynamics, mirroring the nonlinear changes in the physical system's eigenvectors under compression.⁶⁶ Importantly, the NLSF is able to perform the nonlinear mode mixing while maintaining invariance to the intrinsic sign ambiguity of the Laplacian eigenvectors used in the spectral decomposition (see Non-linear Spectral Filter).

The simulators are evaluated on four distinct datasets generated with different algorithms, each consisting of compression trajectories of DENs with Poisson ratios spanning a broad range, including both auxetic networks (systems with negative Poisson ratios)⁶⁷ and non-auxetic ones. We find that nonlinear spectral models predict the dynamics more accurately and with less bias than the widely used spatial models, as well as standard linear spectral GNNs. Importantly, NLSFs exhibit substantially slower performance degradation with increasing rollout length in comparison to both the spatial and the other spectral models. Moreover, they can generate longer, valid rollouts, even when provided with less information in the input. We further investigate how combining a spatial model with a spectral-based models to form a spatio-spectral GNN⁶⁸ affects overall performance. We find that this combined approach can improve the model's overall accuracy in some cases.

II. METHODS

A. Datasets

We test our models on four different datasets with varying dynamics. All datasets consist of compression trajectories. Each trajectory consists of snapshots of the network at different timesteps. The datasets comprise networks exhibiting a wide range of Poisson's ratios ν , spanning both auxetic ($\nu < 0$) and non-auxetic regimes. Details on data generation and representation are provided in the Supplementary Information (SI). Briefly, all networks were generated using a jamming algorithm.⁶⁹ The first dataset hereinafter called "NODE-OPT" was generated using node displacement optimization.⁶⁰ The second was generated using a greedy pruning algorithm and is called "BOND-PRU-OPT."⁵⁷ The third was created by random node displacement and pruning of edges, called "NOI-PRU."⁴⁹ Lastly, we created a dataset that combines all the previous ones, called "COMB."

B. Models

Let G be an undirected graph with node set $[N] = \{1, \dots, N\}$, edges $E \subset [N]^2$, and adjacency matrix $\mathbf{A} = (a_{i,j})_{i,j \in [N]} \in \mathbb{R}^{N \times N}$ where $a_{i,j} = 1$ if $(i, j) \in E$ and $a_{i,j} = 0$ otherwise. Note that since G is undirected, $(i, j) \in E$ iff $(j, i) \in E$, and hence \mathbf{A} is a symmetric matrix. Let $\mathbf{x}_i \in \mathbb{R}^2$ denote the feature at vertex i , representing velocity. We denote by $\mathcal{N}_i = \{j \in [N] \mid (i, j) \in E\}$ the neighborhood of node i . We denote by $\mathbf{X} = (\mathbf{x}_i)_{i=1}^N \in \mathbb{R}^{N \times 2h}$ the array of all node

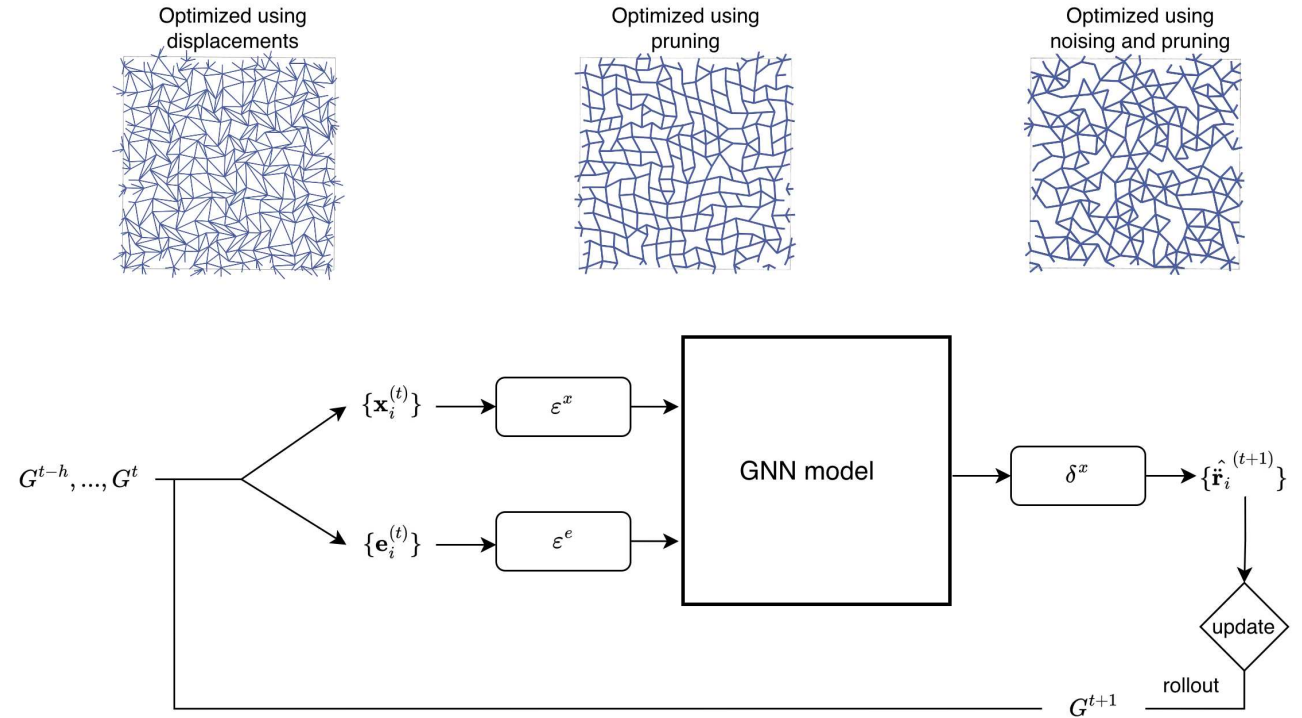


FIG. 1. The simulator model pipeline with an encoder-processor-decoder architecture. ϵ^x, ϵ^e are encoders for the node and edge features, respectively. The GNN block takes the various models defined in the Models section. GNN blocks can be stacked. δ^x is the decoder that maps the output to the accelerations. The update segment constructs the predicted graph from the accelerations. The networks at the top represent samples (left to right) from the datasets "NODE-OPT," "BOND-PRU," and "NOI-PRU, respectively."

features, each as a column vector. h , hereinafter referred to as "history", represents the number of configurations used as input in the training. Likewise, the array of edge features is denoted by $\mathbf{E} = (\mathbf{e}_i)_{i=1}^M \in \mathbb{R}^{N \times 4}$

1. Spatial model

Spatial GNNs are widely used in GNN literature for a variety of tasks, including simulators.^{35,36,55} The spatial model used here is the same model we used in our previous work³⁰ and follows an encoder-processor-decoder architecture.⁷⁰ The encoder maps the input node and edge features of a given graph G into latent vectors, using learnable multi layer perceptrons (MLPs) $\epsilon^x : \mathbb{R}^{N \times 2h} \rightarrow \mathbb{R}^{N \times d}$ and $\epsilon^e : \mathbb{R}^{N \times 4} \rightarrow \mathbb{R}^{N \times d}$ for the node and edge features, respectively. The processor consists of ℓ identical message passing (MP) layers, each with its own set of learnable parameters. These layers are applied sequentially, with each layer operating on the output of the previous one. We denote the node features at layer ℓ by $(\mathbf{x}_i^{(\ell)} \in \mathbb{R}^{d^{(\ell)}})_{i \in [N]}$, where $d^{(\ell)}$ is the latent dimension at layer ℓ . The node features at all layers are computed from the previous layer by

$$\mathbf{x}_i^{(\ell)} = \psi^{(\ell)}(\mathbf{x}_i^{(\ell-1)}), \sum_{j \in \mathcal{N}(i)} \phi^{(\ell)}(\mathbf{x}_i^{(\ell-1)}, \mathbf{x}_j^{(\ell-1)}, \mathbf{e}_{ij}). \quad (1)$$

Here, $\phi^{(\ell)} : \mathbb{R}^{3d^{(\ell-1)}} \rightarrow \mathbb{R}^{d^{(\ell)}}$ is a trainable multilayer per-

ceptron (MLP) called the *message function*, and it is interpreted as a message sent from the neighbor j to node i . In (1), each node i aggregates all received messages by summing them up. Then, a trainable MLP $\psi^{(\ell)} : \mathbb{R}^{d^{(\ell-1)} + c^{(\ell)}} \rightarrow \mathbb{R}^{d^{(\ell)}}$ called the *update function* computes the feature of node i at the next layer. The edge features between node i and j , denoted with \mathbf{e}_{ij} , are shared in all layers and computed from the input positions $\mathbf{r}_i, \mathbf{r}_j$ after each forward pass as follows

$$\mathbf{e}_{ij} = \left(\mathbf{r}_i - \mathbf{r}_j, \|\mathbf{r}_i - \mathbf{r}_j\|_2, \frac{1}{l_0} \right) \in \mathbb{R}^{N \times 4}, \quad (2)$$

where the above denotes a concatenation of four columns, and l_0 is the rest length of the edge. The output of ψ in the last MLP block in the processor is mapped by a decoder $\delta^x : \mathbb{R}^{N \times d} \rightarrow \mathbb{R}^{N \times 2}$ representing the predicted acceleration.

2. Spectral Filters on Graphs

One useful way to represent a graph is via its Laplacian matrix \mathbf{L} . Spectral graph theory states⁷¹ that many properties of a graph can be conveniently expressed in terms of the eigenvectors $\mathbf{V} = \{\mathbf{v}_i\}_{i=1}^N \in \mathbb{R}^{N \times N}$ and eigenvalues $\boldsymbol{\lambda} = \{\lambda_i\}_{i=1}^N \in \mathbb{R}^N$ of its Laplacian. Here, $\mathbf{L} = \mathbf{V}\boldsymbol{\Lambda}\mathbf{V}^\top$, where $\boldsymbol{\Lambda} = \text{diag}(\boldsymbol{\lambda}) \in \mathbb{R}^{N \times N}$ is a diagonal matrix with the eigenvalues filling the di-

agonal entries and 0 otherwise. The eigenvectors in this case are interpreted as the graph Fourier modes, the eigenvalues as the frequencies of the graph, and \mathbf{V}^\top and \mathbf{V} as the graph Fourier transform and its inverse respectively. In this work, we use the symmetric normalized Laplacian

$$\mathbf{L}_{sym} = \mathbf{I} - \mathbf{D}^{-1/2} \mathbf{A} \mathbf{D}^{-1/2}, \quad (3)$$

where $\mathbf{I} \in \mathbb{R}^{N \times N}$ is the identity matrix, and $\mathbf{D} = \text{diag}(d_1, \dots, d_N) \in \mathbb{R}^{N \times N}$ is the degree matrix, where d_i is the number of elements in \mathcal{N}_i . Other definitions of a graph Laplacian are possible but we found that the above representation leads to increased performance compared to others. In addition, this representation is the most common choice in the literature.

Spectral filters extend the idea of convolution to graphs.^{55,64} The classical convolution theorem in Euclidean space states that convolution in space is equivalent to multiplication in frequency. Inspired by this, convolution on graphs is defined as multiplication in the graph frequency. Given frequency responses $\mathbf{f} = (f_1, \dots, f_N)$, the corresponding spectral filter \mathbf{C}_f is defined to be

$$\forall \mathbf{X} \in \mathbb{R}^N, \quad \mathbf{C}_f \mathbf{X} = \mathbf{V} \text{diag}(\mathbf{f})(\mathbf{V}^\top \mathbf{X}). \quad (4)$$

Common GNNs based on spectral filters do not learn the frequency responses $\mathbf{f} \in \mathbb{R}^N$ directly. Instead, one learns a function $q : \mathbb{R} \rightarrow \mathbb{R}$ and defines the frequency responses as $\mathbf{f}_q = (q(\lambda_1), \dots, q(\lambda_N))$. In this case we denote $q(\mathbf{L}) := \mathbf{C}_{\mathbf{f}_q}$. When the node features $\mathbf{X} \in \mathbb{R}^{N \times d}$ are of dimension $d > 1$, the above scheme extends to a frequency response function $Q : \mathbb{R} \rightarrow \mathbb{R}^{d' \times d}$ and a multi-channel spectral filter

$$\forall \mathbf{X} \in \mathbb{R}^{N \times d}, \quad Q(\mathbf{L}) \mathbf{X} := \sum_{i=1}^N \mathbf{v}_i \mathbf{v}_i^\top \mathbf{X} Q(\lambda_i)^\top.$$

Note that $Q(\mathbf{L})$ is a linear operator from $\mathbb{R}^{N \times d}$ to $\mathbb{R}^{N \times d'}$.

Some examples of GNNs based on this scheme are ChebNet⁶⁴ and GCN,⁷² where Q is parameterized as a polynomial, and CayleyNet,⁷³ where Q is a rational function. In this work, we use two different architectures to define Q : as a polynomial via ChebNet⁶⁴, and as a multi-layer-perceptron (MLP), where only the first k leading eigenvectors/values are used.

3. Non-linear Spectral Filter

Non-linear spectral filters (NLSFs) are filters that operate nonlinearly and non-diagonally on the spectral coefficients.⁶⁵ Note that the eigenvectors \mathbf{v}_i are not uniquely defined given \mathbf{L} , but rather only the eigenspaces are unique. For example, both $\pm \mathbf{v}_i$ are eigenvectors of λ_i . Hence, NLSF are designed to be independent of the arbitrary choice of the eigenbasis, and depend only on the eigenspaces and eigenvalues. Consider the graph Fourier inversion formula $\mathbf{X} = \sum_i \mathbf{v}_i \mathbf{v}_i^\top \mathbf{X}$ for $\mathbf{X} \in \mathbb{R}^N$. Here, $\mathbf{v}_i^\top(\mathbf{X})$ is seen as the transformation that computes the

i -th frequency coefficient of \mathbf{X} , also called the *analysis operator*, and $\sum_i \mathbf{v}_i(\mathbf{v}_i^\top \mathbf{X})$ is seen as the inverse transformation, or *synthesis*. A naive nonlinear filter takes the form

$$\Psi(\mathbf{X}) := \sum_i \mathbf{v}_i \psi_i(\mathbf{v}_i^\top \mathbf{X})_{j=1}^N, \quad (5)$$

where $\psi : \mathbb{R}^N \rightarrow \mathbb{R}^N$ is some function, e.g., a MLP, and $\psi_i(\mathbf{v}_i^\top \mathbf{X})_{j=1}^N$ is the i 'th coordinate of the output of ψ on the input $(\mathbf{v}_i^\top \mathbf{X})_{j=1}^N$. However, (5) depends on the arbitrary choice of the sign of the eigenvectors. Instead, NLSF define analysis as $\mathcal{A}(\mathbf{X}) = (|\mathbf{v}_i^\top \mathbf{X}|)_{i=1}^N$ and synthesis of $\mathbf{Y} = (y_j) \in \mathbb{R}^N$ as

$$\mathcal{S}(\mathbf{Y}) = \sum_{i=1}^N \frac{\mathbf{v}_i \mathbf{v}_i^\top \mathbf{X}}{|\mathbf{v}_i^\top \mathbf{X}|} y_i.$$

Here, $\mathbf{v}_i \mathbf{v}_i^\top$ is the projection upon the i 'th eigenspace, and $|\mathbf{v}_i^\top \mathbf{X}|$ is the magnitude of this projection of \mathbf{X} , assuming multiplicity 1 of the eigenvalue λ_i . Note that $\frac{\mathbf{v}_i \mathbf{v}_i^\top \mathbf{X}}{|\mathbf{v}_i^\top \mathbf{X}|}$ is a consistent choice of an eigenvector that depends only on the given data, even though \mathbf{v}_i is an arbitrary choice. The above gives the inversion formula

$$\mathbf{X} = \sum_i \frac{\mathbf{v}_i \mathbf{v}_i^\top \mathbf{X}}{|\mathbf{v}_i^\top \mathbf{X}|} |\mathbf{v}_i^\top \mathbf{X}|.$$

Now, a NLSF is defined as

$$\Psi(\mathbf{X}) := \sum_{i=1}^N \frac{\mathbf{v}_i \mathbf{v}_i^\top \mathbf{X}}{|\mathbf{v}_i^\top \mathbf{X}|} \psi_i(|\mathbf{v}_i^\top \mathbf{X}|)_{j=1}^N,$$

where $\psi : \mathbb{R}^N \rightarrow \mathbb{R}^N$, and $\psi_i(|\mathbf{v}_i^\top \mathbf{X}|)_{j=1}^N$ is the i 'th coordinate of the output of ψ on the input vector $(|\mathbf{v}_i^\top \mathbf{X}|)_{j=1}^N \in \mathbb{R}^N$. The stable extension of this idea to multichannel signals $\mathbf{X} \in \mathbb{R}^{N \times d}$ takes the form

$$\Psi(\mathbf{X}) := \sum_{i=1}^N \left((\mathbf{v}_i \mathbf{v}_i^\top \mathbf{X}) ./ (|\mathbf{v}_i^\top \mathbf{X}| + \epsilon) \right) \psi_i(|\mathbf{v}_i^\top \mathbf{X}|)_{j=1}^N, \quad (6)$$

where $\psi_i : \mathbb{R}^{N \times d} \rightarrow \mathbb{R}^{d \times d'}, i = 1, \dots, N$ are trainable functions, $|\mathbf{v}_i^\top \mathbf{X}| = (|\mathbf{v}_i^\top \mathbf{X}[:, j]|)_{j=1}^d$, and $./$ is elementwise division, and $\epsilon > 0$ is a small constant for stabilizing division by zero. This formulation was extended to any multiplicity of the eigenvalues in the original paper.⁶⁵

The motivation for using nonlinear spectral filters in our context stems not only from their universal approximation capabilities, but also from the physical observation that, in systems under strain or deformation, changes in eigenmodes are governed by interactions among other eigenmodes (see SI Sec.5). NLSFs capture such inter-mode couplings by enabling nonlinear mixing of the frequency coefficients. For more details regarding NLSFs, we refer to the original paper.

We consider a multilayer architecture, where each layer ℓ is of the form

$$\mathbf{X}^{(\ell+1)} := \Psi^{(\ell)}(\mathbf{X}^{(\ell)})$$

where $\Psi^{(\ell)} : \mathbb{R}^{N \times d^{(\ell)}} \rightarrow \mathbb{R}^{N \times d^{(\ell)}}$ is a trainable NLSF model. The NLSF is used within the simulator framework (Fig.1).

In our implementation, we restrict the expressive capacity of the NLSF via

$$\Psi(\mathbf{X}) := \sum_{i=1}^k \left(\frac{\mathbf{v}_i \mathbf{v}_i^\top \mathbf{X}}{\|\mathbf{v}_i^\top \mathbf{X}\|_{\mathbb{R}^d}^\alpha + \epsilon} \right) \psi_i (\|\mathbf{v}_j^\top \mathbf{X}\|_{\mathbb{R}^d})_{j=1}^k, \quad (7)$$

where a norm is taken over the feature direction, instead of taking element-wise absolute value. Here, k represents the first k eigenvectors and $0 < \alpha, \epsilon < 1$ are constants to improve stability. We found that this variant of NLSF improves the generalization performance, possibly due to a reduced ample complexity.

C. Spatio-spectral Models

We also experimented in combining spatial and spectral models to form spatio-spectral models (S^2GNNs).⁴³ See SI (Sec.8) for details.

D. Computational Details

All models were implemented using PyTorch Geometric 2.5.2⁷⁴ and PyTorch 2.2.2.⁷⁵ The simulations were performed using the LAMMPS software package.⁷⁶ For the implementation and data generation details, see SI.

III. RESULTS

Our main objective is to evaluate whether the use of spectral models as simulators can achieve higher accuracy in their auto-regressive predictions of elastic network dynamics than spatial models, and, as a result, produce more stable rollout trajectories, that is, whether they can maintain reasonable predictive accuracy over longer periods of time. To this end, we initially focus on two performance measures: (1) the particles' L_2 positional error at the final step of a rollout, and (2) the model's ability to accurately predict the Poisson ratio of the rollout, which emerges as a macroscopic property of the simulated dynamics. We compute the Poisson ratio $\nu \approx \frac{-D_y}{D_x}$, where D_x, D_y are the strains along each dimension, calculated directly from the node positions (see SI Sec.3). To benchmark our results, we compare the performance of spectral simulators against the spatial baseline model, which is the most widely used approach in the literature for network-structured systems.^{35–38,46}

We conduct our investigation using the four datasets introduced in section II A. We average the obtained results over 4 independently trained models (9 for NOI-PRU and COMB) with different random train/test splits for all four datasets, evaluated at different simulation time steps (Fig.2). Recall that 100 simulator steps correspond roughly to 10,000–50,000 MD steps, depending on network size (see SI, Sec.1 and 5). Importantly, all models were trained only on trajectories of 20 simulation steps, indicating their ability to generalize beyond their training horizon. (We found that training on much longer

Model	NODE-OPT (↓)	COMB (↓)	BOND-PRU-OPT (↓)	NOI-PRU (↓)
Spatio-spectral (NLSF)	0.024 ± 0.0016	0.067 ± 0.010	0.047 ± 0.0016	0.117 ± 0.009
Spatio-spectral (NLSF, norm)	0.021 ± 0.0008	0.052 ± 0.006	0.043 ± 0.0010	0.094 ± 0.004
Spatio-spectral (MLP)	0.023 ± 0.0016	0.077 ± 0.024	0.052 ± 0.0040	0.124 ± 0.019
Spatio-spectral (ChebNet)	0.021 ± 0.0016	0.074 ± 0.016	0.046 ± 0.0050	0.115 ± 0.013
Spatial	0.030 ± 0.0114	0.084 ± 0.023	0.084 ± 0.0180	0.292 ± 0.545
ChebNet	0.020 ± 0.0016	0.076 ± 0.022	<u>0.044 ± 0.0016</u>	0.119 ± 0.019
MLP	0.026 ± 0.0016	0.070 ± 0.012	0.056 ± 0.0024	0.116 ± 0.014
NLSF	0.031 ± 0.0020	0.059 ± 0.012	0.062 ± 0.0020	0.120 ± 0.005
NLSF (norm)	0.026 ± 0.0016	<u>0.058 ± 0.005</u>	0.052 ± 0.0016	<u>0.095 ± 0.003</u>

TABLE I. $L_2[\sigma]$ of the predicted vs. ground truth positions at 50 rollout steps.

trajectories did not improve the Poisson ratio prediction accuracies significantly.)

We begin by testing the linear spectral models, ChebNet and spectral MLP. We observed that these models have a comparable performance to the spatial model, slightly outperforming it on NODE-OPT and BOND-PRU-OPT, while lagging behind it on the NOI-PRU dataset (see Fig.2). This suggests that the linear spectral models cannot better capture the underlying physical patterns of the networks' dynamics, leading to error accumulation and poor generalization when the dynamics become more complex (see Fig.2). In contrast, the norm-NLSF model consistently outperforms all alternatives in predicting the networks' Poisson ratios across all datasets, with particularly strong performance on the NOI-PRU dataset, which is characterized by the most complex dynamics (see Fig.2 & Tables I-II). Here, we note that applying the norm (see Eq.7) instead of the absolute value as originally done⁶⁵ leads to a noticeable increase in performance across all datasets (Tables I and II). We conjecture that using the norm reduces the number of parameters in the model, making it less prone to overfitting.

Interestingly, although the positional prediction errors of the NLSF are sometimes only marginally smaller than those of the spatial and linear spectral models, its Poisson ratio predictions are substantially more accurate. We find that this can be explained by the markedly lower systematic error exhibited by the norm-NLSF model (see Figs. S3 and S4). Furthermore, when projecting node positional errors onto the networks' Laplacian eigenvectors, we observe that the NLSF captures the system's slow modes significantly better than the other models, while showing no major advantage over spatial models in capturing fast modes (see Fig.S5). Taken together, these results indicate that the NLSF more effectively captures the slow, long-range modes of the system, which explains its markedly improved performance in predicting a global property such as the Poisson ratio.

We found out that, in many cases, combining spectral and spatial models improves performance. For instance, a spatio-spectral model using ChebNet as its spectral component on average outperforms ChebNet alone (Tables I and II). A similar trend appears for the spectral MLP, although not uniformly across all datasets. In other words, when the spectral model does not fully capture the system's behavior, the spatial component can compensate for some of its limitations, albeit at the cost of a higher risk of overfitting. By contrast, only marginal gains were observed for the norm-NLSF model, and incor-

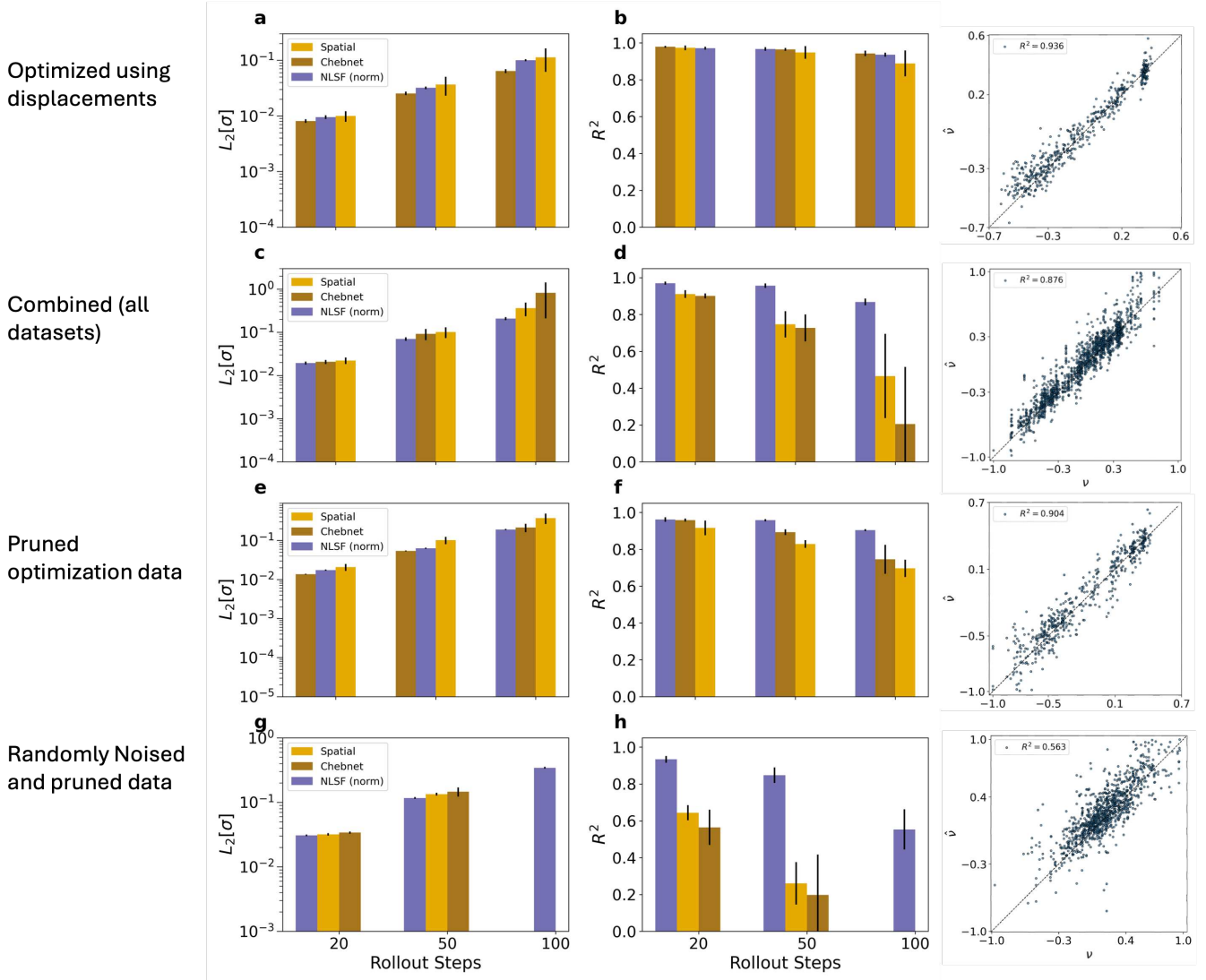


FIG. 2. Performance of the spectral models vs. the spatial model as a function of rollout steps. The first column is the average L_2 over several trials between the predicted positions at each rollout step and the ground truth positions at that step. The second column is the average R^2 over trials of the predicted and ground truth Poisson's ratio at the given rollout steps. The third column contains the parity plots of Poisson's ratio for a norm-NLSF model (the most accurate model), along with its R^2 value as measured at rollout step 100.

Model	NODE-OPT (\uparrow)	COMB (\uparrow)	BOND-PRU-OPT (\uparrow)	NOI-PRU (\uparrow)
Spatio-spectral (NLSF)	0.965 ± 0.013	0.892 ± 0.031	0.933 ± 0.020	0.574 ± 0.117
Spatio-spectral (NLSF, norm)	0.975 ± 0.010	0.953 ± 0.014	0.966 ± 0.008	0.812 ± 0.051
Spatio-spectral (MLP)	0.960 ± 0.006	0.645 ± 0.257	0.871 ± 0.012	0.227 ± 0.166
Spatio-spectral (ChebNet)	0.967 ± 0.007	0.753 ± 0.082	0.882 ± 0.035	0.292 ± 0.198
Spatial	0.948 ± 0.034	0.747 ± 0.072	0.828 ± 0.021	0.234 ± 0.134
ChebNet	0.965 ± 0.008	0.727 ± 0.073	0.893 ± 0.015	0.241 ± 0.189
MLP	0.940 ± 0.009	0.662 ± 0.233	0.801 ± 0.033	0.245 ± 0.175
NLSF	0.954 ± 0.018	0.898 ± 0.024	0.932 ± 0.024	0.654 ± 0.081
NLSF (norm)	0.967 ± 0.010	0.956 ± 0.012	0.957 ± 0.007	0.850 ± 0.041

TABLE II. R^2 of the predicted vs. ground truth Poisson's ratio at 50 rollout steps.

porating a spatial component can even increase overfitting, leading to reduced performance in some cases, e.g. NOI-PRU dataset (Tables I and II). Notably, the NLSF models out-

perform also the spatio-spectral variants built on the spectral MLP and ChebNet (see Tables I and II & Fig.2), with the advantage becoming especially pronounced at longer prediction horizons and the NOI-PRU and BOND-PRU-OPT datasets (see Fig.2).

It was previously shown³⁰ that a key factor influencing the prediction accuracy of spatial GNN models is the number of past configurations supplied in addition to the system's current state. Motivated by this, we examined how the number of such history steps affects the performance of the spectral models (Fig.3). Our results indicate that the norm-NLSF model also performs best in this regard: it requires fewer historical configurations to achieve high accuracy and consistently surpasses the spatial baseline. Moreover, the norm-NLSF exhibits only a weak dependence on history length and is the sole model capable of producing plausible rollouts even with

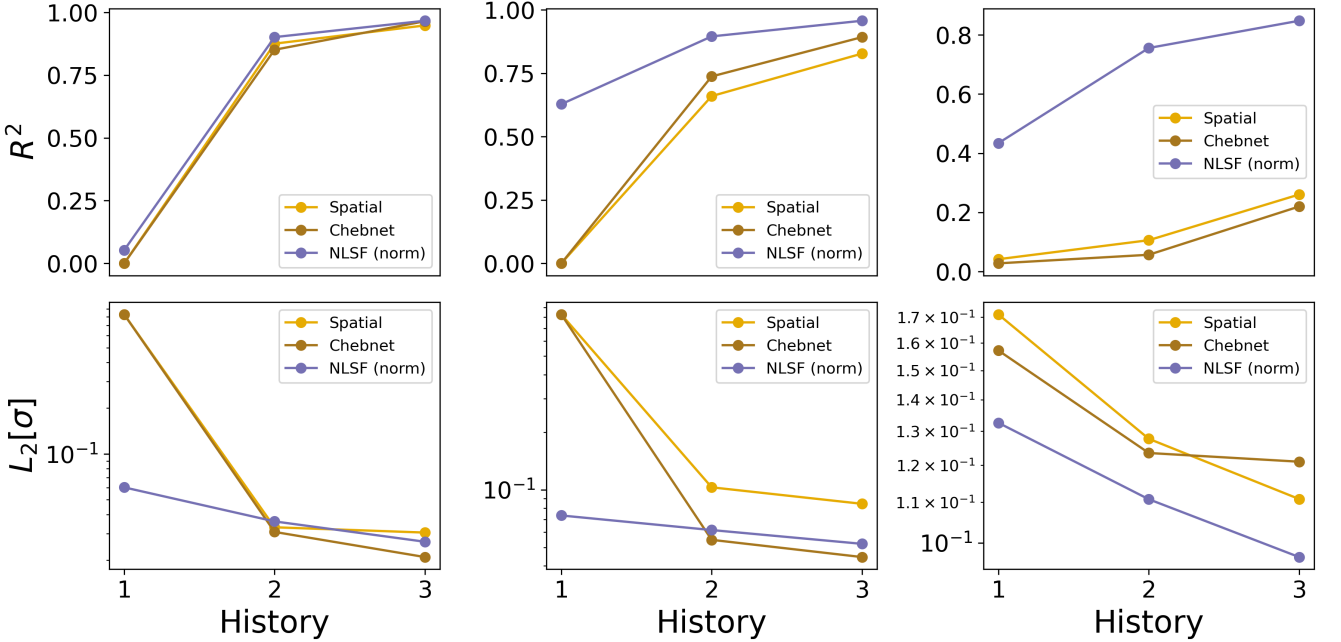


FIG. 3. **Upper row.** From left to right is Average R^2 as a function of history on NODE-OPT, BOND-PRU-OPT, NOI-PRU (from left to right). **Lower row.** From left to right is Average L_2 of the node positions at rollout step 50 as a function of history on NODE-OPT, BOND-PRU-OPT, NOI-PRU. All models were tested on 100 unseen trajectories. If a model's predictions have $R^2 < 0$, we map them all to zero. $L_2 > 1$ are not shown.

$h = 1$. In contrast, the performance of the spatial model deteriorates substantially as the available history is reduced.

Finally, the decline in Poisson ratio prediction accuracy across datasets is also reflected in the individual node trajectory predictions. When examining node-wise motion as a function of rollout length, we observed that the spatial model captures dynamics less accurately, whereas the norm-NLSF model remains closer to the ground truth (see Fig.S2). This difference becomes more apparent as the rollout horizon increases and the underlying dynamics grow more complex, as in the NOI-PRU dataset.

IV. DISCUSSION AND CONCLUSION

In this study, we investigated whether spectral graph neural network (GNN) simulators can overcome the limitations of standard GNN-based simulators in efficiently propagating long-range information by explicitly representing the system in a global eigenmode basis, and thereby better capturing collective and long-range behavior. We found that while spectral representations alone are not sufficient, a nonlinear spectral filter (NLSF) simulator consistently outperforms both commonly used purely spatial GNN simulators and linear spectral-based models across a range of test sets of disordered elastic networks exhibiting diverse dynamical behaviors. Model performance was evaluated based on its ability to accurately predict ground-truth node positions over long rollout horizons, as well as its ability to predict Poisson's ratio as an emergent property and to generalize this prediction to previously unseen

networks.

Across our metrics, that spectral GNNs employing linear filters exceed the spatial baseline only intermittently while NLSFs (and their corresponding spatio-spectral models) showed a uniformly superior performance, outperforming both the spatial model and their spectral counterparts. Notably, although the NLSF achieves only modest improvements in positional accuracy relative to the spatial and linear spectral models, it yields substantially more accurate predictions of the Poisson ratio. This discrepancy can be attributed to the significantly lower systematic error exhibited by the norm-NLSF model (Figs.S3 and S4). Moreover, analysis in the Laplacian eigenbasis reveals that the NLSF captures the system's slow modes far more effectively than the other approaches (Fig.S5). These findings demonstrate that the strength of the NLSF lies in its ability to represent slow, long-range dynamics, which in turn underpins its superior performance in predicting global physical properties such as the Poisson ratio.

We further observed that NLSFs can achieve higher accuracy than both the purely spatial and linear spectral models with fewer history steps, while still producing rollout trajectories longer than those used during training. This can be viewed as another indication that the effective inclusion of global spatial information of the network can make up for the lack of temporal information.

This performance boost highlights the importance of capturing both global and local information within simulator models, as well as enabling nonlinear mixing of the spectral decomposition coefficients, mirroring, in this study's case, the nonlinear changes in the physical systems' eigenvectors un-

der compression. It is worth noting that the graph Laplacian closely resembles the “response force” (or stiffness) matrix of elastic networks, which encodes how a system responds to strain. Motivated by this, we also experimented with using the networks’ stiffness matrix in place of the symmetric Laplacian, since it incorporates the actual bond stiffness values rather than unit weights. However, we found that the symmetric graph Laplacian yielded better performance. This may be because the variation in bond stiffness values is relatively small, so including them did not add essential information for dynamic prediction and instead introduced additional noise into the learning process.

The accuracy achieved by NLSFs demonstrates a promising pathway for enhancing both the precision and rollout stability of GNN-based simulators. These results open new opportunities for applying such models in high-throughput screening, dynamic optimization tasks that require accurate trajectory prediction, and inverse design applications.

V. SUPPLEMENTARY INFORMATION

The supplementary information includes details on the data generation (Sec.1), dataset information (Sec.2), Poisson’s ratio estimation (Sec.3), details about the simulator framework (Sec.4) derivation of the eigenvectors and values under compression (Sec.5), and step translation (Sec.6), implementation details (Sec.7), details on spatio-spectral models (Sec.8), and comparison plots for individual node trajectories (Sec.9), and bias and error plots (Sec.10).

ACKNOWLEDGMENTS

The authors acknowledge support from the Israel Science Foundation (ISF) under grant number 1181/24. RL is supported by a grant from the United States-Israel Binational Science Foundation (BSF), Jerusalem, Israel, and the United States National Science Foundation (NSF), (NSF-BSF, grant No. 2024660), and by the Israel Science Foundation (ISF grant No. 1937/23).

DATA AVAILABILITY

Data used in this work is available upon request.

REFERENCES

- M. Mowbray, T. Savage, C. Wu, Z. Song, B. A. Cho, E. A. Del Rio Chanona, and D. Zhang, “Machine learning for biochemical engineering: A review,” *Biochemical Engineering Journal* **172**, 1369–703 (2021).
- H. Liu, Z. Fu, K. Yang, X. Xu, and M. Bauchy, “Machine learning for glass science and engineering: A review,” *Journal of Non-Crystalline Solids* **557**, 119419 (2021).
- H. Wang, T. Fu, Y. Du, W. Gao, K. Huang, Z. Liu, P. Chandak, S. Liu, P. Van Katwyk, A. Deac, A. Anandkumar, K. Bergen, C. P. Gomes, S. Ho, P. Kohli, J. Lasenby, J. Leskovec, T. Y. Liu, A. Manrai, D. Marks, B. Ramsundar, L. Song, J. Sun, J. Tang, P. Veličković, M. Welling, L. Zhang, C. W. Coley, Y. Bengio, and M. Zitnik, “Scientific discovery in the age of artificial intelligence,” *Nature* **620**, 47–60 (2023).
- P. Notin, N. Rollins, Y. Gal, C. Sander, and D. Marks, “Machine learning for functional protein design,” *Nature Biotechnology* **42**, 216–228 (2024).
- J. Behler and M. Parrinello, “Generalized neural-network representation of high-dimensional potential-energy surfaces,” *Physical Review Letters* **98** (2007), 10.1103/PhysRevLett.98.146401.
- P. M. Piaggi, A. Selloni, A. Z. Panagiotopoulos, R. Car, and P. G. Debenedetti, “A first-principles machine-learning force field for heterogeneous ice nucleation on microcline feldspar,” *Faraday Discussions* **249**, 98–113 (2024).
- L. Zhang, H. Wang, M. C. Muniz, A. Z. Panagiotopoulos, R. Car, and E. Weinan, “A deep potential model with long-range electrostatic interactions,” *Journal of Chemical Physics* **156**, 124107 (2022).
- A. P. Bartók, J. Kermode, N. Bernstein, and G. Csányi, “Machine Learning a General-Purpose Interatomic Potential for Silicon,” *Physical Review X* **8**, 041048 (2018).
- J. Zhang, L. Bonati, E. Trizio, O. Zhang, Y. Kang, T. Hou, and M. Parrinello, “Descriptor-Free Collective Variables from Geometric Graph Neural Networks,” *Journal of Chemical Theory and Computation* **20**, 10787–10797 (2024).
- L. Bonati, G. M. Piccini, and M. Parrinello, “Deep learning the slow modes for rare events sampling,” *Proceedings of the National Academy of Sciences of the United States of America* **118**, e2113533118 (2021).
- L. Bonati, E. Trizio, A. Rizzi, and M. Parrinello, “A unified framework for machine learning collective variables for enhanced sampling simulations: mlcolvar,” *Journal of Chemical Physics* **159** (2023), 10.1063/5.0156343.
- V. Rizzi, D. Mendels, E. Sicilia, and M. Parrinello, “Blind Search for Complex Chemical Pathways Using Harmonic Linear Discriminant Analysis,” *Journal of Chemical Theory and Computation* **15**, 4507–4515 (2019).
- D. Mendels, G. Piccini, Z. F. Brotzakis, Y. I. Yang, and M. Parrinello, “Folding a small protein using harmonic linear discriminant analysis,” *Journal of Chemical Physics* **149**, 194113 (2018).
- D. Mendels, G. Piccini, and M. Parrinello, “Collective Variables from Local Fluctuations,” *Journal of Physical Chemistry Letters* **9**, 2776–2781 (2018).
- G. Piccini, D. Mendels, and M. Parrinello, “Metadynamics with Discriminants: A Tool for Understanding Chemistry,” *Journal of Chemical Theory and Computation* **14**, 5040–5044 (2018).
- F. Noé, S. Olsson, J. Köhler, and H. Wu, “Boltzmann generators: Sampling equilibrium states of many-body systems with deep learning,” *Science* **365** (2019), 10.1126/science.aaw1147.
- Z. F. Brotzakis, D. Mendels, and M. Parrinello, “Augmented Harmonic Linear Discriminant Analysis,” (2019).
- S. A. Hollingsworth and R. O. Dror, “Molecular Dynamics Simulation for All,” *Neuron* **99**, 1129–1143 (2018).
- S. S. Chong, Y. S. Ng, H. Q. Wang, and J. C. Zheng, “Advances of machine learning in materials science: Ideas and techniques,” *Frontiers of Physics* **19**, 13501 (2024).
- X. Zhang, L. Wang, J. Helwig, Y. Luo, C. Fu, Y. Xie, M. Liu, Y. Lin, Z. Xu, K. Yan, K. Adams, M. Weiler, X. Li, T. Fu, Y. Wang, A. Strasser, H. Yu, Y. Xie, X. Fu, S. Xu, Y. Liu, Y. Du, A. Saxton, H. Ling, H. Lawrence, H. Stärk, S. Gui, C. Edwards, N. Gao, A. Ladera, T. Wu, E. F. Hofgard, A. M. Tehrani, R. Wang, A. Daigavane, M. Bohde, J. Kurtin, Q. Huang, T. Phung, M. Xu, C. K. Joshi, S. V. Mathis, K. Azizzadenesheli, A. Fang, A. Aspuru-Guzik, E. Bekkers, M. Bronstein, M. Zitnik, A. Anandkumar, S. Ermon, P. Liò, R. Yu, S. Gunnemann, J. Leskovec, H. Ji, J. Sun, R. Barzilay, T. Jaakkola, C. W. Coley, X. Qian, X. Qian, T. Smidt, and S. Ji, “Artificial Intelligence for Science in Quantum, Atomistic, and Continuum Systems,” *Foundations and Trends® in Machine Learning* **18**, 385–912 (2025).
- P. Avery, X. Wang, C. Oses, E. Gossett, D. M. Proserpio, C. Toher, S. Curtarolo, and E. Zurek, “Predicting superhard materials via a machine learning informed evolutionary structure search,” *npj Computational Materials* **5**, 89 (2019).
- J. Ojih, A. Rodriguez, J. Hu, and M. Hu, “Screening outstanding mechanical properties and low lattice thermal conductivity using global attention graph neural network,” *Energy and AI* **14** (2023), 10.1016/j.egyai.2023.100286.

²³Z. Yao, B. Sánchez-Lengeling, N. S. Bobbitt, B. J. Bucior, S. G. H. Kumar, S. P. Collins, T. Burns, T. K. Woo, O. K. Farha, R. Q. Snurr, and A. Aspuru-Guzik, “Inverse design of nanoporous crystalline reticular materials with deep generative models,” *Nature Machine Intelligence* **3**, 76–86 (2021).

²⁴Z. Liu, D. Zhu, S. P. Rodrigues, K. T. Lee, and W. Cai, “Generative Model for the Inverse Design of Metasurfaces,” *Nano Letters* **18**, 6570–6576 (2018).

²⁵J. H. Bastek and D. M. Kochmann, “Inverse design of nonlinear mechanical metamaterials via video denoising diffusion models,” *Nature Machine Intelligence* **5**, 1466–1475 (2023).

²⁶M. Zu and C. P. Goodrich, “Designing athermal disordered solids with automatic differentiation,” *Communications Materials* **5**, 141 (2024).

²⁷M. Zu, A. Desai, and C. P. Goodrich, “Fully Independent Response in Disordered Solids,” *Physical Review Letters* **134**, 238201 (2025).

²⁸D. Mendels and J. J. De Pablo, “Collective Variables for Free Energy Surface Tailoring: Understanding and Modifying Functionality in Systems Dominated by Rare Events,” *Journal of Physical Chemistry Letters* **13**, 2830–2837 (2022).

²⁹D. Mendels, F. Bylén, T. W. Sirk, and J. J. de Pablo, “Systematic modification of functionality in disordered elastic networks through free energy surface tailoring,” *Science Advances* **9** (2023), 10.1126/sciadv.adf7541.

³⁰S. N. Salman, S. A. Shteingolts, R. Levie, and D. Mendels, “Evaluating the use of a machine learning simulator for structure–property prediction: A case study on disordered elastic networks,” *The Journal of Chemical Physics* **163** (2025), 10.1063/5.0282871.

³¹J. Colen, M. Han, R. Zhang, S. A. Redford, L. M. Lemma, L. Morgan, P. V. Ruijgrok, R. Adkins, Z. Bryant, Z. Dogic, M. L. Gardel, J. J. de Pablo, and V. Vitelli, “Machine learning active-nematic hydrodynamics,” *Proceedings of the National Academy of Sciences of the United States of America* **118** (2021), 10.1073/pnas.2016708118.

³²S. Wiewel, M. Becher, and N. Thuey, “Latent Space Physics: Towards Learning the Temporal Evolution of Fluid Flow,” *Computer Graphics Forum* **38**, 71–82 (2019).

³³L. Ladický, S. Jeong, B. Solenthaler, M. Pollefeys, and M. Gross, “Data-driven Fluid Simulations using Regression Forests,” *ACM Transactions on Graphics* **34** (2015), 10.1145/2816795.2818129.

³⁴D. Kochkov, J. A. Smith, A. Alieva, Q. Wang, M. P. Brenner, and S. Hoyer, “Machine learning–accelerated computational fluid dynamics,” *Proceedings of the National Academy of Sciences of the United States of America* **118**, 1–4 (2021).

³⁵A. Sanchez-Gonzalez, J. Godwin, T. Pfaff, R. Ying, J. Leskovec, and P. W. Battaglia, “Learning to simulate complex physics with graph networks,” *37th International Conference on Machine Learning, ICML 2020 Part F16814*, 8428–8437 (2020).

³⁶T. Pfaff, M. Fortunato, A. Sanchez-Gonzalez, and P. W. Battaglia, “Learning Mesh-Based Simulation with Graph Networks,” *ICLR 2021 - 9th International Conference on Learning Representations*, 1–18 (2020).

³⁷H. Liu, Z. Huang, S. S. Schoenholz, E. D. Cubuk, M. M. Smedskjaer, Y. Sun, W. Wang, and M. Bauchy, “Learning molecular dynamics: predicting the dynamics of glasses by a machine learning simulator,” *Materials Horizons* **10**, 3416–3428 (2023).

³⁸K. Kumar and J. Vantassel, “GNS: A generalizable Graph Neural Network-based simulator for particulate and fluid modeling,” *Journal of Open Source Software* **8**, 5025 (2023).

³⁹Z. Li, J. Cen, L. Wu, H. Sun, H. Mao, zhangfuzheng, D. ZHANG, and W. Huang, “Geometric Spatiotemporal Transformer to Simulate Long-Term Physical Dynamics,” (2025).

⁴⁰B. Ummenhofer, L. Prantl, N. Thuey, and V. Koltun, “Lagrangian Fluid Simulation with Continuous Convolutions,” in *International Conference on Learning Representations* (2020).

⁴¹F. Bigi, S. Chong, A. Kristiadi, and M. Ceriotti, “FlashMD: long-stride, universal prediction of molecular dynamics,” (2025).

⁴²F. L. Thiemann, T. Reschützegger, M. Esposito, T. Tadese, J. D. Olarte-Plata, and F. Martelli, “Force-Free Molecular Dynamics Through Autoregressive Equivariant Networks,” (2025).

⁴³F. Ge and P. O. Dral, “Artificial Intelligence for Direct Prediction of Molecular Dynamics Across Chemical Space,” (2025).

⁴⁴M. Xu, J. Han, A. Lou, J. Kossaifi, A. Ramanathan, K. Azizzadenesheli, J. Leskovec, S. Ermon, and A. Anandkumar, “Equivariant Graph Neural Operator for Modeling 3D Dynamics,” (2024).

⁴⁵M. Schreiner, O. Winther, and S. Olsson, “Implicit Transfer Operator Learning: Multiple Time-Resolution Surrogates for Molecular Dynamics,” (2023).

⁴⁶Z. Li, K. Meidani, P. Yadav, and A. Barati Farimani, “Graph neural networks accelerated molecular dynamics,” *Journal of Chemical Physics* **156** (2022), 10.1063/5.0083060.

⁴⁷T. Xie, A. France-Lanord, Y. Wang, J. Lopez, M. A. Stolberg, M. Hill, G. M. Leverick, R. Gomez-Bombarelli, J. A. Johnson, Y. Shao-Horn, and J. C. Grossman, “Accelerating amorphous polymer electrolyte screening by learning to reduce errors in molecular dynamics simulated properties,” *Nature Communications* **13**, 3415 (2022).

⁴⁸R. Newbury, J. Collins, K. He, J. Pan, I. Posner, D. Howard, and A. Cosgun, “A Review of Differentiable Simulators,” *IEEE Access* **12**, 97581–97604 (2024).

⁴⁹D. Dold and D. Aranguren van Egmond, “Differentiable graph-structured models for inverse design of lattice materials,” *Cell Reports Physical Science* **4**, 101586 (2023).

⁵⁰F. Scarselli, M. Gori, A. C. Tsoi, M. Hagenbuchner, and G. Monfardini, “The graph neural network model,” *IEEE Transactions on Neural Networks* **20**, 61–80 (2009).

⁵¹M. Cranmer, A. Sanchez-Gonzalez, P. Battaglia, R. Xu, K. Cranmer, D. Spergel, and S. Ho, “Discovering symbolic models from deep learning with inductive biases,” *Advances in Neural Information Processing Systems 2020-Decem*, 1–25 (2020).

⁵²K. Yang, Y. Huang, J. Tao, W. Wang, and Q. Wu, “Physics-Inspired All-Pair Interaction Learning for 3D Dynamics Modeling,” (2025).

⁵³Q. Li, Z. Han, and X.-M. Wu, “Deeper Insights into Graph Convolutional Networks for Semi-Supervised Learning,” (2018).

⁵⁴U. Alon and E. Yahav, “On the Bottleneck of Graph Neural Networks and its Practical Implications,” (2021).

⁵⁵D. Bo, X. Wang, Y. Liu, Y. Fang, Y. Li, and C. Shi, “A Survey on Spectral Graph Neural Networks,” (2023).

⁵⁶E. Lerner, E. Degiuli, G. Düring, and M. Wyart, “Breakdown of continuum elasticity in amorphous solids,” *Soft Matter* **10**, 5085–5092 (2014).

⁵⁷D. R. Reid, N. Pashine, J. M. Wozniak, H. M. Jaeger, A. J. Liu, S. R. Nagel, and J. J. De Pablo, “Auxetic metamaterials from disordered networks,” *Proceedings of the National Academy of Sciences of the United States of America* **115**, E1384–E1390 (2018).

⁵⁸M. L. Manning, “Rigidity in mechanical biological networks,” *Current biology : CB* **34**, R1024–R1030 (2024).

⁵⁹M. Berneman and D. Hexner, “Designing precise dynamical steady states in disordered networks,” (2024).

⁶⁰M. Shen, M. A. Reyes-Martinez, L. A. Powell, M. A. Iadicola, A. Sharma, F. Bylén, N. Pashine, E. P. Chan, C. L. Soles, H. M. Jaeger, and J. J. de Pablo, “An autonomous design algorithm to experimentally realize three-dimensionally isotropic auxetic network structures without compromising density,” *npj Computational Materials* **10**, 113 (2024).

⁶¹M. Stern, D. Hexner, J. W. Rocks, and A. J. Liu, “Supervised Learning in Physical Networks: From Machine Learning to Learning Machines,” *Physical Review X* **11**, 021045 (2021).

⁶²M. Stern and A. Murugan, “Learning Without Neurons in Physical Systems,” *Annual Review of Condensed Matter Physics* **14**, 417–441 (2023).

⁶³I. Bahar, T. R. Lezon, L. W. Yang, and E. Eyal, “Global dynamics of proteins: Bridging between structure and function,” *Annual Review of Biophysics* **39**, 23–42 (2010).

⁶⁴M. Defferrard, X. Bresson, and P. Vandergheynst, “Convolutional Neural Networks on Graphs with Fast Localized Spectral Filtering,” in *Advances in Neural Information Processing Systems*, Vol. 29, edited by D. Lee, M. Sugiyama, U. Luxburg, I. Guyon, and R. Garnett (Curran Associates, Inc., 2016).

⁶⁵Y.-W. E. Lin, R. Talmon, and R. Levie, “Equivariant Machine Learning on Graphs with Nonlinear Spectral Filters,” (2024).

⁶⁶L. D. Landau and E. M. Lifshitz, *Quantum mechanics: non-relativistic theory*, Vol. 3 (Elsevier, 2013).

⁶⁷R. Lakes, “Foam Structures with a Negative Poisson’s Ratio,” *Science* **235**, 1038–1040 (1987).

⁶⁸S. Geisler, A. Kosmala, D. Herbst, and S. Günemann, “Spatio-Spectral Graph Neural Networks,” (2024).

⁶⁹A. J. Liu and S. R. Nagel, “The jamming transition and the marginally jammed solid,” *Annual Review of Condensed Matter Physics* **1**, 347–369

(2010).

⁷⁰J. B. Hamrick, K. R. Allen, V. Bapst, T. Zhu, K. R. McKee, J. B. Tenenbaum, and P. W. Battaglia, “Relational inductive bias for physical construction in humans and machines,” *Proceedings of the 40th Annual Meeting of the Cognitive Science Society, CogSci 2018* , 1773–1778 (2018).

⁷¹F. R. K. Chung, *Spectral graph theory*, Vol. 92 (American Mathematical Soc., 1997).

⁷²T. N. Kipf and M. Welling, “Semi-Supervised Classification with Graph Convolutional Networks,” (2017).

⁷³R. Levie, F. Monti, X. Bresson, and M. M. Bronstein, “CayleyNets: Graph Convolutional Neural Networks with Complex Rational Spectral Filters,” (2018).

⁷⁴M. Fey and J. E. Lenssen, “Fast Graph Representation Learning with PyTorch Geometric,” (2019).

⁷⁵A. Paszke, S. Gross, F. Massa, A. Lerer, J. Bradbury, G. Chanan, T. Killeen, Z. Lin, N. Gimelshein, L. Antiga, A. Desmaison, A. K. Narlak, E. Yang, Z. DeVito, M. Raison, A. Tejani, S. Chilamkurthy, Q. Ai, B. Steiner, L. F. Fang, J. B. Bai, S. Chintala, “PyTorch: An imperative style, high-performance deep learning library. In *Advances in Neural Information Processing Systems*,” *NeurIPS* , 8026–8037 (2019).

⁷⁶A. P. Thompson, H. M. Aktulga, R. Berger, D. S. Bolintineanu, W. M. Brown, P. S. Crozier, P. J. in ’t Veld, A. Kohlmeyer, S. G. Moore, T. D. Nguyen, R. Shan, M. J. Stevens, J. Tranchida, C. Trott, and S. J. Plimpton, “LAMMPS - a flexible simulation tool for particle-based materials modeling at the atomic, meso, and continuum scales,” *Computer Physics Communications* **271**, 108171 (2022).

Supporting Information for a Non Linear Spectral Graph Neural Network Simulator for More Stable and Accurate Rollouts

Salman N. Salman,^{1, a)} Sergey A. Shteingolts,^{1, a)} Ron Levie,² and Dan Mendels^{1, b)}

¹⁾*The Wolfson Department of Chemical Engineering, Technion – Israel Institute of Technology, Haifa 32000, Israel*

²⁾*Faculty of Mathematics, Technion – Israel Institute of Technology, Haifa 32000, Israel*

^{a)}These authors contributed equally to this work.

^{b)}E-mail: danmendels@technion.ac.il

I. DETAILS ON TRAINING DATA GENERATION

1. *On unit conversion*

For our systems, the following fundamental quantities were chosen: The distance unit σ was defined as an average bond length of all the DENs in the dataset, m was the beads' mass and ϵ was set to be the average bond constant (see below). Hereinafter, all quantities are listed in these units.

A. Elastic Network Generation

Disordered elastic networks (DENs) were generated in a two-step process.¹ First, N soft disks of four different types and diameters were placed randomly in equal proportions in a simulation box with periodic boundary conditions and allowed to relax to a local energy minimum using a standard jamming algorithm.² The frictional force between each pair of disks located within a contact distance $d = R_i + R_j$ is responsible for interaction:

$$F = (k_n \delta \mathbf{n}_{ij} - m_{eff} \gamma_n \mathbf{v}_n) - (k_t \Delta s_t + m_{eff} \gamma_t \mathbf{v}_t), \quad (1)$$

where δ is an overlap distance of two disks, \mathbf{n}_{ij} is the unit vector along the line connecting the centers of two disks, k_n and k_t are elastic constants for normal and tangential contact, respectively, γ_n and γ_t are viscoelastic constants for normal and tangential contact, $m_{eff} = \frac{M_i M_j}{M_i + M_j}$ is an effective mass of two disks i and j with individual masses M_i and M_j , \mathbf{v}_n and \mathbf{v}_t are the normal and tangential components of the relative velocity of the two disks, and Δs_t is the tangential displacement vector between the two disks. In our cases, k_t , γ_n and γ_t were set to zero, while k_n was set to 1.0, so the resulting force between the two disks is simply expressed as follows:

$$F = \delta \mathbf{n}_{ij} \quad (2)$$

During the energy minimization, the system was slowly cooled from $T_{start} = 5 \times 10^{-6}$ to $T_{end} = 1 \times 10^{-6}$. After that, the beads were placed at the center of each disk and harmonic bonds were created between those beads that were in contact with each other, with the contact distance defined as the sum of disks' radii $d_{ij} = R_i + R_j$. Harmonic bonds were assigned an elastic energy in the form:

$$E(r_{ij}) = K_b (l - l_{re})^2, \quad (3)$$

where K_b is the bond coefficient with units *energy/distance*², l_{re} is the bond rest length, and l is the distance between the two beads. For each bond, the value of K_b was set to $1/l_{re}$. The resulting network configuration was then scanned for "dangling" beads, i.e., those with less than 3 connections to their neighbors, and those dangling beads were removed from the network. This procedure was applied iteratively until no such beads were left. To include angle-bending constraints, for each pair of bonds sharing one common bead an angle with an harmonic potential was assigned, with the energy in the form:

$$E(\theta_{km}) = K_{ang}(\theta_{km} - \theta_{km}^0)^2, \quad (4)$$

where K_{ang} is the angle coefficients for angle θ_{km} between the pair of edges k and m , and θ_{km}^0 is the rest angle. For the final dataset, K_{ang} was set to 0 which further enhanced the networks' dynamics complexity and the model's ability to generalize.

1. *Uniaxial compression simulation*

Compression simulations of the 2d DENs were carried out using LAMMPS³ molecular dynamics simulator. The systems were simulated within the NPT ensemble with anisotropic pressure control (applied to the simulation box in the direction perpendicular to compression), with constant temperature $T = 1 \times 10^{-10}$, $k_B = 1$, damping parameter of 7.1×10^{-3} and time step $\tau = 7.13 \times 10^{-6}$ controlled by the Langevin thermostat.⁴ The compression was simulated using the **fix deform** command of LAMMPS with a constant strain rate $s_r = 1 \times 10^{-8}$ and the maximum strain not exceeding 5% of the initial box dimension along the compressed axis. Constant zero-pressure along the non-compressed axis was applied on the simulation box perpendicular to the direction of compression using the Parrinello-Rahman barostat,⁵ which allowed the simulation box to change volume based on the mechanical properties of the network.

B. Auxetic Networks

1. *Generating networks for NODE-OPT*

For the first dataset, networks with low Poisson values were generated by optimizing previously generated high Poisson value networks (obtained with the methodology described above) using the

global node optimization strategy⁶ implemented in Python 3.2.12 using a custom-written code. The algorithm is based on gradient descent and aims to minimize Poisson's ratio ν by altering individual node positions. At each iteration n , the coordinate of each node i , \mathbf{r}_i is displaced one by one by 5×10^{-4} in an axis $\eta \in \{x, y\}$, the bond lengths and angles are recalculated accordingly. Then, ν for the resulting network configuration is measured (see section IB 4) and the gradient is computed:

$$\frac{\partial(\nu + \mathcal{L}_1 + \mathcal{L}_2)}{\partial r_{i\eta}}, \quad (5)$$

where $r_{i\eta}$ is the displacement of node i in the axis η , while \mathcal{L}_1 and \mathcal{L}_2 are the internode distance and angle constraints, respectively, which are defined as follows:

$$\mathcal{L}_1 = 0.1 \sum_{i,j} H(r_{min} - r_{ij})(r_{ij} - r_{min})^2, \quad (6)$$

$$\mathcal{L}_2 = 0.01 \sum_j H(\theta_{min} - \theta_j)(\theta_j - \theta_{min})^6, \quad (7)$$

where H is the Heaviside step function, while r_{min} and θ_{min} are the minimal values for bond distances and angles, respectively. The latter were chosen by trial and error, with the final values set to 0.2 and 15°. To prevent structure from changing too aggressively and make the optimization process more stable, gradients were clipped to 0.01 by absolute value. Finally, the initial node positions are updated using the $N \times 2$ gradient matrix obtained at the previous step:

$$r_{i\eta}^{n+1} = r_{i\eta}^n + \lambda \frac{\partial(\nu + \mathcal{L}_1 + \mathcal{L}_2)}{\partial r_{i\eta}}, \quad (8)$$

where λ is the learning rate, which was set to 4. The process is repeated iteratively until either *a*) the desired target value for ν is reached or *b*) the number of iterations exceeds the maximum of 50.

2. Generating networks for BOND-PRU-OPT

Auxetic networks were generated using the iterative bond pruning strategy described in⁷, which relies on individual bond-level response to compression and targeted modification of shear to bulk modulus ratio G/B . At each iteration of the process, a trial removal of each bond is performed, and its effect on G is recorded. The bond removal which caused the smallest change in shear modulus ΔG is then pruned from the network completely. This procedure tends to increase G/B ratio and

decrease Poisson's ratio ν , defined as the negative ratio of transverse strain to axial strain:

$$\nu = -\frac{\epsilon_{trans}}{\epsilon_{axial}} \quad (9)$$

3. Generating networks for NOI-PRU

This approach is inspired by a procedure used in another publication.⁸ We begin by non-auxetic networks that were generated with the jamming algorithm. The procedure works as follows:

1. We select a random set of nodes from the graph and noise them slightly using Gaussian noise.
2. Then, we pick a random set of edges from the same graph and prune them, including the nodes connected to them.
3. these networks are then compressed and their Poisson's ratios are recorded.

4. Elastic moduli

Elastic moduli were computed using LAMMPS molecular dynamics simulator. A compression simulation with a small strain $\epsilon = 1 \times 10^{-4}$ was performed and corresponding elastic constants C_{ij} were calculated. For two-dimensional isotropic systems, such as the 2d disordered elastic networks considered here, the elastic tensor is represented by a 3×3 matrix, which contains three independent elastic constants C_{ij} due to the symmetry constraints of an isotropic material: C_{11} , C_{12} and C_{66} . These relate the stress along i axis to the strain along j axis as follows: $\sigma_i = C_{ij} \cdot \epsilon_j$. Since the studied networks were not completely isotropic, as a precaution elastic constants C_{11} and C_{12} were calculated as averages, e.g., $C_{11}^a = (C_{11} + C_{22})/2$. From this, the desired elastic moduli were calculated as follows:

$$B = (C_{11}^a + C_{12}^a)/2 \quad (10)$$

$$G = (C_{11}^a - C_{12}^a)/2 \quad (11)$$

$$\nu = \frac{(1 - G/B)}{(1 + G/B)} \quad (12)$$

II. DATA DESCRIPTION AND REPRESENTATION

A. Datasets

Each dataset contains auxetic and non-auxetic networks. The networks were generated using a jamming algorithm.² The networks' range of Poisson's ratios was either attained through optimization or random pruning of the edges and random displacements of the nodes. For the first dataset, hereinafter called "NODE-OPT," the network's distribution of Poisson's ratios spanned the range $\nu \in [-0.4, 0.6]$. The auxetic networks in this dataset were generated using the global optimization algorithm.⁶ The second dataset, hereinafter called "BOND-PRU-OPT," including networks with Poisson's ratios spanning the range $\nu \in [-0.9, 0.6]$, was constructed using optimization carried out using a greedy pruning procedure.⁷ The networks in the third dataset, termed "NOI-PRU," which were found to exhibit the most complex compression dynamics among all datasets, were generated by randomly perturbing the node positions and randomly pruning edges. ⁸ The range of Poisson's ratio for this dataset was $\nu \in [-0.2, 0.6]$. The final dataset, termed "COMB," was constructed by combining the three datasets described above, spanning a Poisson ratio range of $\nu \in [-0.9, 0.6]$.

B. Data Representation

Each timestep in the trajectory is encoded into G , containing a set of node features \mathbf{X} and edge features \mathbf{E} . Each graph node corresponds to an elastic network particle and has an associated one-dimensional feature vector \mathbf{x}_i , containing information about the node velocity, calculated as $\mathbf{r}_i^t = \mathbf{r}_i^t - \mathbf{r}_i^{t-1}$, where \mathbf{r}_i^t is the i -th node position at time t and \mathbf{r}_i^{t-1} its position at time $t - 1$. More generally, node velocity vectors can be of the dimension \mathbb{R}^{2h} , with h referring to the number of previous history configuration to be included in the model's input. The edge features in the graph describe the bonded interactions between particles. For each graph edge \mathbf{e}_{ij} representing a bond between particles i and j , the corresponding features are $\mathbf{r}_i - \mathbf{r}_j$, the length l of the edge vector and a stiffness factor that determines the strength of the bond.

III. POISSON'S RATIO ESTIMATION

To evaluate the model's predictive power, we estimate the Poisson's ratio for the model rollout using the following expression:

$$v_{est} = -D_y/D_x, \quad (13)$$

where D is the approximation for simulation box change at time t with respect to time 0:

$$D_\eta = l_\eta^0 \times \frac{\sum_{i=1}^N |r_\eta^t|}{\sum_{i=1}^N |r_\eta^0|} - l_\eta^0, \quad (14)$$

where l_η^0 is the simulation box size in the η dimension at the beginning of compression, $|r_\eta^0|$ and $|r_\eta^t|$ the distances between each node i and the simulation box center $(0, 0)$ at the first and the last rollout steps, respectively, and N the number of nodes in the network. While not strictly accurate, this procedure provides a good enough estimation, with errors not exceeding 5%.

IV. SIMULATOR

The neural network simulator is the general framework we use to predict the dynamics. It has an encoder-processor-decoder architecture.^{9,10} The encoders and decoders learnable functions. The model used to implement the processor block varies, but the general pipeline remains the same regardless of the model. The simulator's objective is to predict the next configuration in an elastic network compression trajectory based on the system's previous configuration/s. It operates in an auto-regressive manner to generate a rollout from the input configurations. In our case, we choose velocity \mathbf{r}^t as input and acceleration at the next-time step as output $\hat{\mathbf{r}}^{t+1}$ but other inputs (e.g. positions) and outputs (e.g. velocities) are also valid. In general, using the accelerations as output yields the best results.^{11,12} The predicted accelerations are then used in a forward Euler integration to obtain the next-step positions $\hat{\mathbf{r}}^{t+1}$ while the edge features are accordingly updated after each such prediction as well. During the training, we minimize the loss between the ground truth next-step acceleration $\hat{\mathbf{r}}^{t+1}$ and the model's predicted acceleration $\hat{\mathbf{r}}^{t+1}$

V. PERTURBATION THEORY

When glassy systems (in our case represented through the disordered elastic networks) are deformed, their mechanical response to a small deformation γ is governed by changes in the strain-

dependent Hessian matrix¹³

$$H(\gamma) = \frac{\partial^2 U(\gamma)}{\partial x^2}, \quad (15)$$

where U is the potential energy and x denotes the particle's Cartesian coordinates. Solving the Hessian eigenproblem

$$H(\gamma)v_i(\gamma) = \lambda_i(\gamma)v_i(\gamma) \quad (16)$$

yields eigenvalues $\lambda_i(\gamma)$ and eigenvectors $v_i(\gamma)$ that define the system's response to deformation. Perturbation theory¹⁴ provides a mathematical understanding of how these modes change under small strains. For a small perturbation $\delta H(\gamma)$ from the local energy minimum strain γ^0 , the first-order approximation is given by

$$\delta\lambda_i = v_i(\gamma^0)^\top \delta H(\gamma)v_i(\gamma^0) \quad (17)$$

$$\delta v_i = \sum_{j \neq i} \frac{v_j(\gamma^0)^\top \delta H(\gamma)v_i(\gamma^0)}{\lambda_i(\gamma^0) - \lambda_j(\gamma^0)} v_j(\gamma^0). \quad (18)$$

VI. STEP TRANSLATION

Each dataset entry corresponds to a compression trajectory comprising a sequence of system configurations sampled from a ground truth simulation at regular timesteps t_s , beginning from the initial timestep $t = 0$. To facilitate the learning process, the sampling periods were adjusted to maintain consistent per-step node velocities across different system sizes. Specifically, the sampling period ξ for each simulation was determined according to:

$$\xi = \frac{\Delta l_t}{s_r l^0}, \quad (19)$$

where Δl_t denotes the constant change in box size along the compression axis between consecutive snapshots across all simulations, s_r is the strain rate, and l^0 is the initial box length along the compression axis.

VII. IMPLEMENTATION

The simulator takes the velocities \mathbf{r}^t and predicts the next-step acceleration $\hat{\mathbf{r}}^t$, where the loss minimizes the differences between $\hat{\mathbf{r}}^t$ and the ground truth acceleration \mathbf{r}^t using the mean-square-error (MSE) as a loss function. All features were normalized to zero mean and unit variance. Each

dataset was split into training and test set. The training ran for 100 epochs. Generally, we found that we only need 50-100 trajectories to obtain accurate prediction on the test data, which consists of 100 unseen trajectories. In this work, we train all models on 100 trajectories. Previously,¹¹ we found out that for the spatial model it is not necessary to train on all the available timesteps in a trajectory; it suffices to consider the first 10-20 steps from each trajectory to get accurate results, which reduces the computational cost significantly. This is the approach we follow here as well, and we use the first 20 steps in each trajectory. The learnable functions were implemented with linear layers, with hidden dimensions of 128 and ReLU activations (SiLU¹⁵ for the spectral encoders). The output for MLP and NLSF filters are normalized by LayerNorm. Unless stated otherwise, all the models were trained with history $h = 3$ and $\ell = 2$. For ChebNet, we have $K = 5$ as the degree of the Chebyshev polynomials, and the eigenvalue cutoff k for the MLP and nonlinear filters is set to 10. All encoders transforms the features from their original size to 128 while the decoders maps back the output features of the processor layer into the output acceleration $\hat{\mathbf{r}}^t \in \mathbb{R}^{N \times 2}$. Decoders in the spectral models consist only of linear layers (since we found this yields a slightly better performance than adding a nonlinearity) while in the spatial model they are implemented using MLPs.

VIII. SPATIO-SPECTRAL MODELS

The idea of spatio-spectral models (S^2GNNs) on graphs was recently introduced, and it aims to circumvent the limitations of spatial GNNs.¹⁶ In this paradigm, the model is split into two branches, spatial and spectral. The spatial part learns the local behavior from local neighborhoods, while the long-range interactions are learned by parameterizing a spectral filter on a truncated eigendecomposition. The final output can be any combination of these outputs. In this work, the final output of the spatio-spectral layer is defined as the sum of the spectral and spatial components, i.e. $\mathbf{X}_{spectral} + \mathbf{X}_{spatial}$. Throughout this work, we use the spatial model in Eq.?? to implement the spatial component of the model, while the spectral part will vary depending on the filter. All spatio-spectral models are used within the simulator’s framework (see Fig.S1).

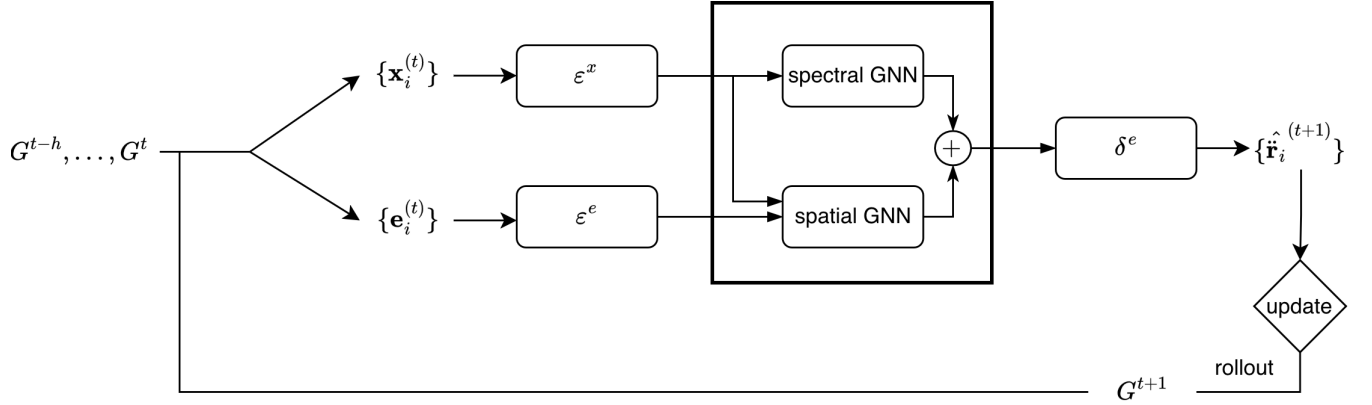


FIG. S1. Spatio-spectral model architecture

IX. DYNAMICS

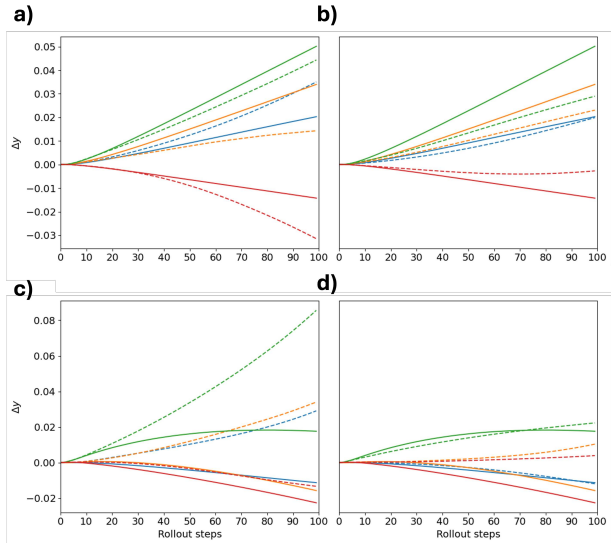


FIG. S2. Prediction (dashed) of randomly selected node trajectories against the ground truth (lines) on BOND-PRU-OPT with norm NLSF model (b) and spatial (a), and on NOI-PRU with norm NLSF (b) and spatial (d).

X. BIAS AND ERROR

For a graph, we define the positional bias as

$$b_\alpha = |\hat{\mathbf{r}}_\alpha| - |\mathbf{r}_\alpha| \quad (20)$$

where \mathbf{r}_α represent the ground positions of the nodes in the graph along coordinate α and $\hat{\mathbf{r}}_\alpha$ are the predicted positions in same coordinate. b_α gives the direction w.r.t the center of the box. If the prediction is underestimated, we get a negative bias while overshooting the target results in a positive bias. As can be seen below, the bias for NOI-PRU is three times smaller in the y axis. To measure how well the eigenmodes are learned we project the positional error w.r.t to the box's center, defined as $|\hat{\mathbf{r}}| - |\mathbf{r}|$, where $\hat{\mathbf{r}}, \mathbf{r} \in \mathbb{R}^{N \times 2}$ are the predicted and ground truth coordinates, respectively. This error is then projected to the frequency space using the eigenvectors.

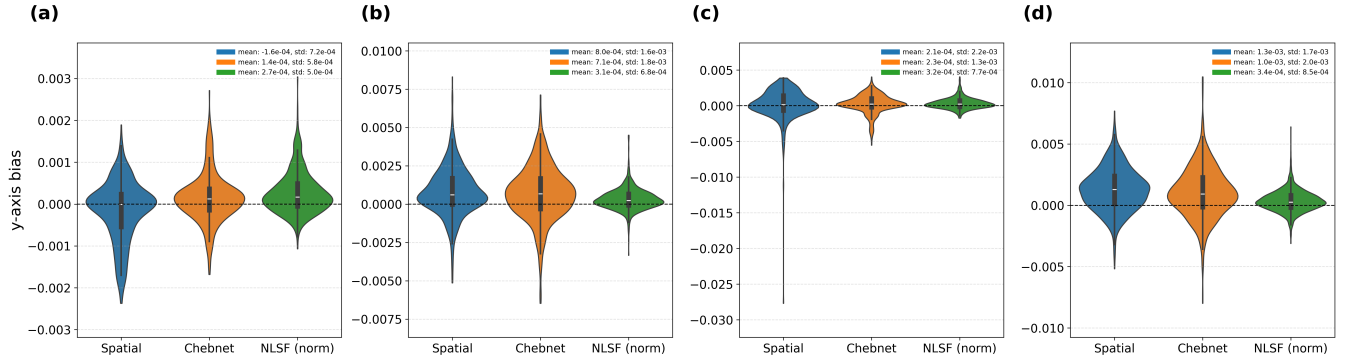


FIG. S3. Positional bias across different datasets for the y axis. In the plot (a) is NODE-OPT (b) is COMB (c) is BOND-PRU-OPT, and (d) is NOI-PRU

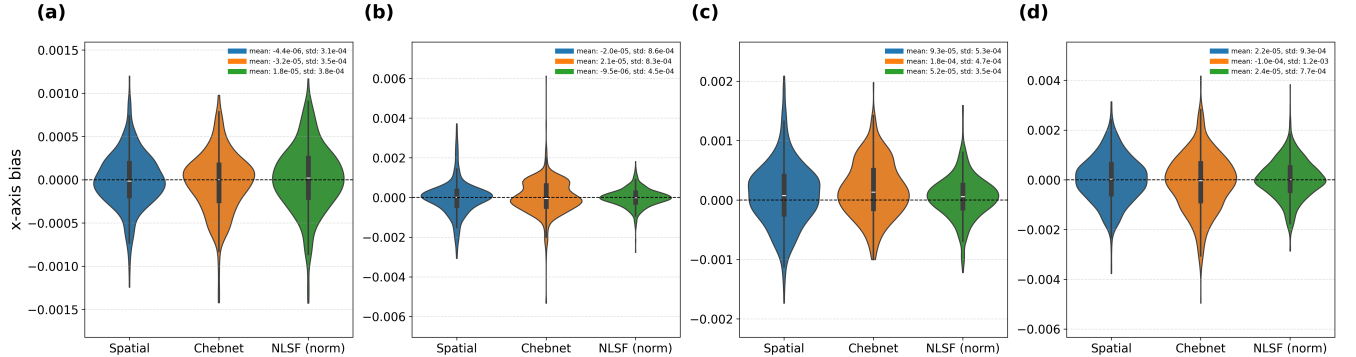


FIG. S4. Positional bias across different datasets for the x axis. In the plot (a) is NODE-OPT (b) is COMB (c) is BOND-PRU-OPT, and (d) is NOI-PRU

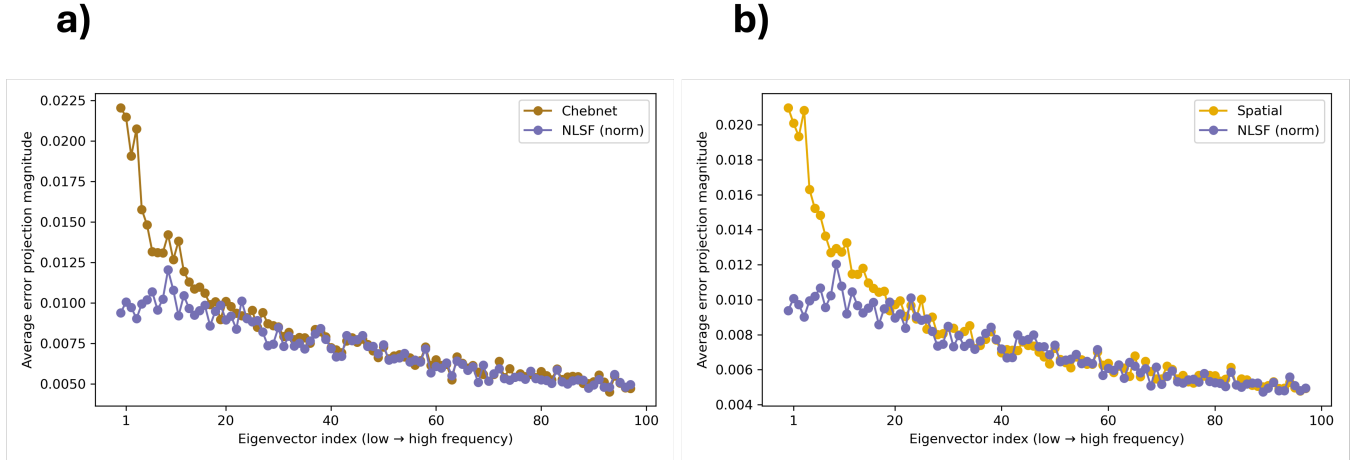


FIG. S5. Projection of the positional error to the frequency space for one seed on NOI-PRU. The norm-NLSF model is compared with ChebNet (a) and the spatial model (b).

REFERENCES

- ¹J. W. Rocks, N. Pashine, I. Bischofberger, C. P. Goodrich, A. J. Liu, and S. R. Nagel, “Designing allosteric response in mechanical networks,” *Proceedings of the National Academy of Sciences of the United States of America* **114**, 2520–2525 (2017).
- ²A. J. Liu and S. R. Nagel, “The jamming transition and the marginally jammed solid,” *Annual Review of Condensed Matter Physics* **1**, 347–369 (2010).
- ³A. P. Thompson, H. M. Aktulga, R. Berger, D. S. Bolintineanu, W. M. Brown, P. S. Crozier, P. J. in ’t Veld, A. Kohlmeyer, S. G. Moore, T. D. Nguyen, R. Shan, M. J. Stevens, J. Tranchida, C. Trott, and S. J. Plimpton, “LAMMPS - a flexible simulation tool for particle-based materials modeling at the atomic, meso, and continuum scales,” *Computer Physics Communications* **271**, 108171 (2022).
- ⁴T. Schneider and E. Stoll, “Molecular-dynamics study of a three-dimensional one-component model for distortive phase transitions,” *Physical Review B* **17**, 1302–1322 (1978).
- ⁵M. Parrinello and A. Rahman, “Polymorphic transitions in single crystals: A new molecular dynamics method,” *Journal of Applied Physics* **52**, 7182–7190 (1981).
- ⁶M. Shen, M. A. Reyes-Martinez, L. A. Powell, M. A. Iadicola, A. Sharma, F. Bylén, N. Pashine, E. P. Chan, C. L. Soles, H. M. Jaeger, and J. J. de Pablo, “An autonomous design algorithm to experimentally realize three-dimensionally isotropic auxetic network structures without com-

promising density,” *npj Computational Materials* **10**, 113 (2024).

⁷D. R. Reid, N. Pashine, J. M. Wozniak, H. M. Jaeger, A. J. Liu, S. R. Nagel, and J. J. De Pablo, “Auxetic metamaterials from disordered networks,” *Proceedings of the National Academy of Sciences of the United States of America* **115**, E1384–E1390 (2018).

⁸D. Dold and D. Aranguren van Egmond, “Differentiable graph-structured models for inverse design of lattice materials,” *Cell Reports Physical Science* **4**, 101586 (2023).

⁹J. B. Hamrick, K. R. Allen, V. Bapst, T. Zhu, K. R. McKee, J. B. Tenenbaum, and P. W. Battaglia, “Relational inductive bias for physical construction in humans and machines,” *Proceedings of the 40th Annual Meeting of the Cognitive Science Society, CogSci 2018* , 1773–1778 (2018).

¹⁰T. Pfaff, M. Fortunato, A. Sanchez-Gonzalez, and P. W. Battaglia, “Learning Mesh-Based Simulation with Graph Networks,” *ICLR 2021 - 9th International Conference on Learning Representations* , 1–18 (2020).

¹¹S. N. Salman, S. A. Shteingolts, R. Levie, and D. Mendels, “Evaluating the use of a machine learning simulator for structure–property prediction: A case study on disordered elastic networks,” *The Journal of Chemical Physics* **163** (2025), 10.1063/5.0282871.

¹²A. Sanchez-Gonzalez, J. Godwin, T. Pfaff, R. Ying, J. Leskovec, and P. W. Battaglia, “Learning to simulate complex physics with graph networks,” *37th International Conference on Machine Learning, ICML 2020 PartF16814*, 8428–8437 (2020).

¹³J. R. López-Blanco, O. Miyashita, F. Tama, and P. Chacón, “Normal Mode Analysis Techniques in Structural Biology,” in *Encyclopedia of Life Sciences* (Wiley, 2014).

¹⁴L. D. Landau and E. M. Lifshitz, *Quantum mechanics: non-relativistic theory*, Vol. 3 (Elsevier, 2013).

¹⁵S. Elfwing, E. Uchibe, and K. Doya, “Sigmoid-weighted linear units for neural network function approximation in reinforcement learning,” *Neural Networks* **107**, 3–11 (2018).

¹⁶S. Geisler, A. Kosmala, D. Herbst, and S. Günnemann, “Spatio-Spectral Graph Neural Networks,” (2024).